Coastal trapped waves and tidal mixing control primary production in the tropical Angolan upwelling system

Mareike Körner, Peter Brandt, Serena Illig, Marcus Dengler, Ajit Subramaniam, Marie-Lou Bachèlery, Gerd Krahmann

To cite this version:

Mareike Körner, Peter Brandt, Serena Illig, Marcus Dengler, Ajit Subramaniam, et al.. Coastal trapped waves and tidal mixing control primary production in the tropical Angolan upwelling system. Science Advances , 2024, 10 (4), 10.1126/sciadv.adj6686 . ird-04559059

HAL Id: ird-04559059
https://ird.hal.science/ird-04559059v1

Submitted on 5 May 2024

SCIENCE ADVANCES | RESEARCH ARTICLE

OCEANOGRAPHY

Coastal trapped waves and tidal mixing control primary production in the tropical Angolan upwelling system

Mareike Körner[1]*, Peter Brandt[1,2], Serena Illig[3,4], Marcus Dengler[1], Ajit Subramaniam[5], Marie-Lou Bachèlery[6], Gerd Krahmann[1]

Eastern boundary upwelling systems are hotspots of marine life and primary production. The strength and seasonality of upwelling in these systems are usually related to local wind forcing. However, in some tropical upwelling systems, seasonal maxima of productivity occur when upwelling favorable winds are weak. Here, we show that in the tropical Angolan upwelling system (tAUS), the seasonal productivity maximum is due to the combined effect of coastal trapped waves (CTWs) and elevated tidal mixing on the shelf. During austral winter, the passage of an upwelling CTW displaces the nitracline upward by more than 50 m. Thereby, nitrate-rich waters spread onto the shelf, where elevated vertical mixing causes a nitrate flux into the surface mixed layer. Interannual variability of the productivity maximum is strongly correlated to the amplitude of the upwelling CTW as seen in sea level data. Given that CTWs are connected to equatorial forcing, a predictability of the strength of the productivity maximum is suggested.

INTRODUCTION

The eastern boundary regions of the tropical Atlantic and Pacific oceans host highly productive ecosystems. These tropical upwelling systems represent a biodiverse marine environment and support one of the most productive marine food chains (*1*–*4*). They are of great importance for local and global fisheries and are affected by interannual climate variability and climate warming (*5*, *6*). It is therefore of great interest to understand the processes that drive these systems. In most tropical upwelling regions, wind stress maxima and productivity maxima are disjoint (Fig. 1, B and C) (*7*, *8*). Thus, processes other than offshore Ekman transport must be the dominant drivers of productivity in these regions. Physical factors discussed in this context are the equatorial current system, surface heat fluxes, remote forcing along the equatorial waveguide, and the mixed layer depth (*8*–*10*). Along with understanding the drivers of the tropical upwelling system, it is of great socioeconomic interest to predict their variability. The coastal tropical upwelling system in the Pacific and Atlantic Ocean exhibits a pronounced seasonal cycle, with important interannual variations superimposed (*11*–*13*). Note that state-of-the-art climate models have difficulties to realistically represent eastern boundary upwelling regions and their variability (*14*–*16*). Large warm biases in sea surface temperature (SST) are still present in the tropical eastern boundary upwelling systems (*14*), suggesting that the physical processes driving these systems are not fully captured in these models. It is crucial to advance process understanding and improve prediction skills to assess possible future changes within these systems, e.g., due to anthropogenic influences.

In this study, we focus on the physical drivers of productivity in the tropical Angolan upwelling system (tAUS) in the Atlantic Ocean. Angolan waters are located between the Congo River outflow at 6°S and the Angola-Benguela frontal zone at ~17°S (Fig. 1).

The tAUS is closely connected to equatorial dynamics. Zonal wind fluctuations at the equator excite equatorial Kelvin waves (EKWs), which propagate eastward, and upon encountering the eastern boundary, part of their energy is transformed into poleward propagating coastal trapped waves (CTWs) (Fig. 1A) (*17*, *18*). CTWs exhibit signals in sea level anomaly (SLA) where upwelling (downwelling) CTWs are associated with a depression (elevation) in sea level. Poleward propagating CTWs not only modulate the near-coastal sea level, but depending on stratification and the local shelf and continental slope topography, they are also associated with specific spatial patterns of velocity and density anomalies. CTWs can be separated into different wave modes, with lower modes propagating faster and exhibiting larger cross-shelf and vertical scales of variability than higher modes (*17*, *19*–*23*).

The seasonal cycle of SLA reveals that two equatorially forced downwelling and two equatorially forced upwelling CTWs propagate along the Angolan coast throughout the year (Fig. 1B) (*9*, *18*, *24*). These waves differ in amplitude. The signal of the main downwelling CTW is visible in February, followed by the main upwelling CTW peaking in July. In October/November, the secondary downwelling CTW propagates along the coast, followed by a secondary upwelling CTW in December/January. The seasonal cycle of CTWs in the tAUS can thus be explained by a superposition of annual and semi-annual harmonics (*9*, *24*, *25*). The dominance of the annual and semi-annual cycle is related to the dominant wind forcing in the equatorial Atlantic and to the basin resonance, relatively enhancing the semi-annual cycle (*26*–*28*).

Productivity also shows variability on the semi-annual cycle (Fig. 1B). The highest net primary production (NPP) is found in July–September during the main upwelling season. A secondary upwelling season is observed in February, which is weaker and restricted to the northern part of the tAUS. Thus, productivity peaks about 1 month after the passage of the upwelling CTWs. Previous studies have discussed whether phytoplankton blooms are forced by CTWs, highlighting that productivity and the occurrence of upwelling CTWs are in phase (*9*, *13*, *29*–*31*). However, the control on productivity by the upwelling CTWs is still not resolved (*13*). Note that the wind-driven upwelling in the tAUS is in general weak

---

[1]GEOMAR Helmholtz Centre for Ocean Research Kiel, Kiel, Germany. [2]Faculty of Mathematics and Natural Sciences, Kiel University, Kiel, Germany. [3]Laboratoire d'Etudes en Géophysique et Océanographie Spatiale (LEGOS), CNRS/IRD/UT3/CNES, Toulouse, France. [4]Department of Oceanography, University of Cape Town, Cape Town, South Africa. [5]Lamont-Doherty Earth Observatory, Columbia University, New York, NY, USA. [6]Geophysical Institute, University of Bergen and Bjerknes Centre for Climate Research, Bergen, Norway.
*Corresponding author. Email: mkoerner@geomar.de

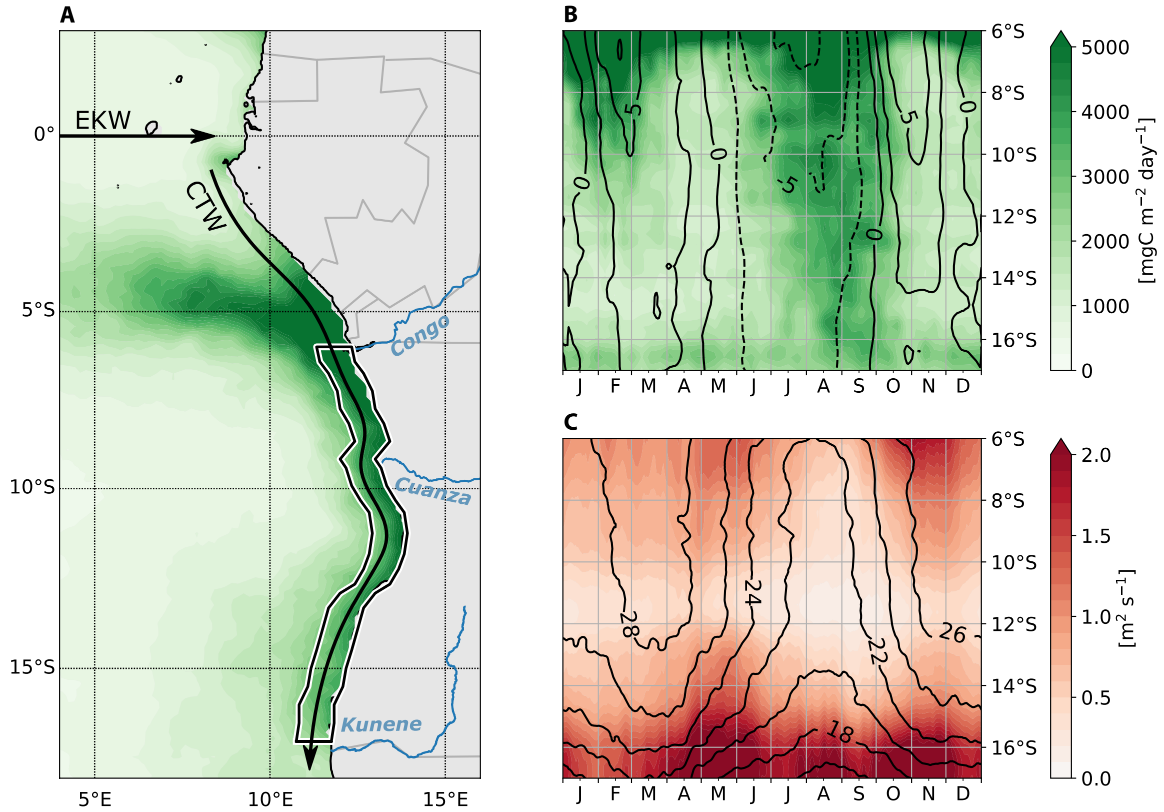

Fig. 1. Primary production and wind-driven upwelling in the tropical Angolan upwelling system. (**A**) Mean net primary production (NPP) in July–September. Black arrows mark the waveguide for equatorial Kelvin waves (EKWs) and coastal trapped waves (CTWs). The solid black box marks the tropical Angolan upwelling system (tAUS). (**B**) Hovmoeller plot showing the seasonal cycle of NPP (colors) and sea level anomaly (SLA) zonally averaged in the coastal box marked in (A) [black contour lines, solid lines positive and dashed lines negative SLA (cm)]. (**C**) Colors show the seasonal cycle of the integrated wind-driven upwelling transport from the coast to one degree offshore representing the sum of Ekman and of wind stress curl–driven upwelling (see Materials and Methods). Black contour lines show the seasonal cycle of the sea surface temperature (°C) zonally averaged in the coastal box marked in (A).

and peaks in May and can thus not explain the seasonal cycle in NPP (Fig. 1C). Further note that in the Peruvian upwelling system, where wind stress maxima and productivity maxima are also disjoint, the seasonal cycle of productivity is discussed to be related to the seasonality of the mixed layer depth with shallowest mixed layer depths during the maxima in productivity (*10*, *12*). This mechanism that involves vertical dilution of phytoplankton and light limitation during periods of deep mixed layer cannot explain the productivity in the tAUS because in contrast to the Peruvian upwelling system the mixed layer depth is deepest during the main productivity season (*32*).

In the Angolan and Benguela upwelling systems, extreme warm and cold events, the so-called Benguela Niños and Benguela Niñas, are the dominant mode of SST variability on interannual timescales (*33*). This interannual variability peaks seasonally during the main downwelling season, between March and April (*34*–*37*), and thus plays a minor role in the productivity variability during the main upwelling season of the tAUS. While Benguela Niños and Benguela Niñas have been related to equatorially forced CTWs (*34*, *38*, *39*), local mechanisms also modulate the strength of these extreme events (*40*, *41*).

In general, CTWs affect ecosystem productivity in multiple ways. One way is through their ability to vertically displace the nitracline. A modeling study conducted on the Peruvian upwelling system showed how equatorially forced intraseasonal CTWs of higher modes can induce phytoplankton blooms by vertically advecting the nitracline into the euphotic zone (*42*). CTWs can also influence biogeochemical conditions through horizontal advection. Observations collected during an intraseasonal CTW event off the coast of Peru showed how nitrate-rich waters were transported along the coast by a low-mode downwelling CTW (*43*).

In the tAUS, the role of vertical mixing, as a mechanism for upward nitrate supply, has been discussed on the basis of the investigated turbulent heat flux (*13*, *29*). The primary energy source for turbulence on the shelf of the tAUS is thought to be the dissipation of internal tidal energy (*31*). The interaction of the barotropic tide with the continental slope leads to the generation of internal tides that partly propagate onto the continental shelf and dissipate in shallow water (*31*). Elevated dissipation rates of turbulent kinetic energy (TKE) are frequently observed in shallow waters on the Angolan shelf, which are responsible for the near-shore cooling of surface waters (*31*, *32*). The regionally confined enhanced mixing on the shelf was associated with breaking internal waves, resulting in the development of frontal structures that leads to the aggregation of small pelagic fish (*44*). However, the role of vertical mixing in the upward supply of nitrate in the tAUS has not been explicitly investigated so far.

In this study, we use hydrographic, oxygen, nitrate, ocean turbulence, and satellite data to analyze the physical drivers of seasonal and interannual variability of NPP in the tAUS. Additionally, we use a regional ocean model to corroborate the observational results. We find that CTWs and enhanced vertical mixing in the water column above the upper continental slope and shelf can explain productivity variability on both seasonal and interannual timescales.

RESULTS

Seasonal changes in nitrate and density

In the tAUS, primary production undergoes a distinct seasonal cycle (Fig. 1B). NPP is elevated during the main upwelling season in late austral winter (July–September) and low during the downwelling phases (February–April/October–December). NPP is limited by nitrate in this region (*45*, *46*). Therefore, to understand the seasonal differences in NPP, the seasonal distribution of nitrate is analyzed. We make use of an extensive dataset of conductivity-temperature-depth (CTD) and oxygen profiles collected between 1995 and 2022 (*9*). From in situ nitrate measurements in the tAUS, we derive a statistical relationship between the apparent oxygen consumption and nitrate (see Materials and Methods). This allows us to use oxygen concentrations to estimate nitrate distributions and analyze their spatial and temporal variability. Most of the data were collected during either the main downwelling season (February–April) or the main upwelling season (July–September).

The cross-shelf sections of inferred nitrate concentration calculated from data between 10°S and 12°S during these two seasons reveal distinct differences (Fig. 2). Nitrate concentrations in the upper ocean are much higher during the upwelling phase than during the downwelling phase. During the upwelling season, nitrate-rich water penetrates far onto the shelf, whereas during the downwelling season, the shelf is mostly covered by low-nitrate waters. Additionally, the upward displacement of nitrate-rich waters during the upwelling season results in a strengthening of the vertical nitrate gradient in the upper ocean.

The upward-displaced nitracline during the upwelling seasons is associated with concurrent upward-displaced isopycnal surfaces (Fig. 2). During both seasons, the position of the nitracline is located foremost between the 25.7 and 26 kg m^{-3} isopycnals. Both isopycnals experience elevated vertical displacements. From the downwelling to the upwelling season, the 25.7 kg m^{-3} isopycnal is displaced by about 42 m, while the 26 kg m^{-3} isopycnal is displaced by 62 m. Figure 2 additionally shows the mixed layer depth during both seasons. On average, it is 11.3 m deep during the main upwelling season and thus slightly deeper than during the main downwelling season (on average 9.1 m).

The large vertical movement of the density surfaces and the nitracline raises the question of what causes this seasonal deformation of the nitrate and density fields. To answer this question, we examine the seasonal density fields closely. The most striking differences in the mean potential density fields are visible near the surface (Fig. 3, A to C). During the downwelling phase, low-density water occupies the upper 40 m of the ocean, resulting in a strongly enhanced upper ocean stratification. In contrast, during the upwelling season, we find denser water near the surface, resulting in a weaker stratification below the mixed layer. These differences in the upper ocean can be explained by surface heat and freshwater fluxes, as well as river runoff, resulting in warmer and fresher surface waters during the downwelling season compared to the upwelling season (*9*, *13*, *32*, *47*). Temperature differences are determined by the seasonal cycle of surface heat fluxes (*32*), while changes in salinity are mainly influenced by the advection of fresh water from the Congo River by the southward flowing Angola Current (*47*). The strength of the Angola Current, and thus the strength of the freshwater advection, is modulated by the different phases of the semi-annual CTWs propagating southward along the Angolan coast. Peaks in southward freshwater advection are in phase with the downwelling CTWs in February/March and October/November. The low-salinity signal in the surface waters weakens southward due to vertical salt advection and mixing at the base of the mixed layer (*47*).

Away from the surface, the density field also exhibits seasonal changes that cannot be explained by surface heat and freshwater fluxes. Figure 3 (A and B) reveals that the 26 kg m^{-3} isopycnal moves upward from the downwelling to the upwelling season, while the depth of the 26.8 kg m^{-3} isopycnal is nearly constant and the 27.05 kg m^{-3} isopycnal moves downward. Thus, the seasonal changes in the density field are depth dependent: Between the surface and about

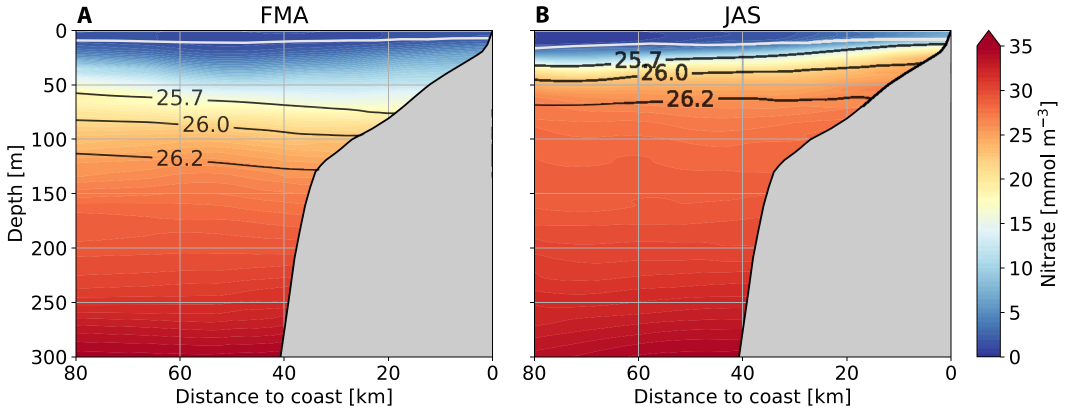

Fig. 2. Cross-shelf sections of nitrate during the downwelling and upwelling season. Cross-shelf sections of nitrate concentration inferred from oxygen data (see Materials and Methods) as a function of distance to the coast. Data collected between 10°S and 12°S are projected onto the mean topography in this latitude band (see Materials and Methods). Mean section for February–April (**A**) and July–September (**B**). Black lines show selected isolines of the mean potential density field. White lines show the mixed layer depth.

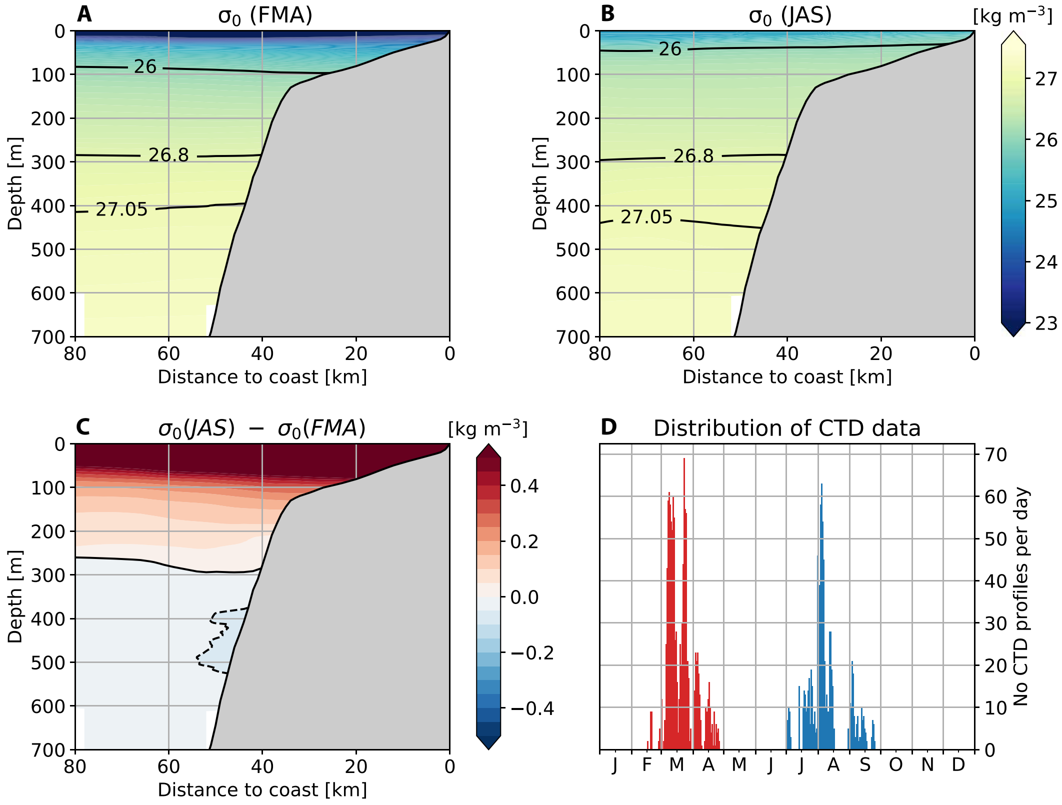

Fig. 3. Cross-shelf sections of potential density during the downwelling and upwelling season. Cross-shelf sections of potential density calculated from CTD data measured between 10°S and 12°S and projected onto the mean topography for February–April (**A**) and July–September (**B**). Black lines show selected isolines of potential density to illustrate seasonal differences. (**C**) Difference between the density fields of both seasons. The solid black line marks the zero contour, and the dashed black line marks the −0.05 kg m^{-3} contour. (**D**) Seasonal distribution of the CTD profiles used in (A) to (C).

300-m depth, the potential density surfaces move upward or outcrop from the downwelling to the upwelling season, while between 300 and 700 m, the potential density surfaces move downward (Fig. 3, A to C). Note that both the upward and downward displacements are larger near the topography than further offshore at the same depth.

One possible mechanism that affects the depth of the density surfaces is wind-driven upwelling. However, the seasonality of the wind-driven upwelling does not match the seasonality of the vertical movements of density surface, i.e., wind-driven upwelling is found to be weakest during the upwelling season (Fig. 1C) (*29*). Another dynamic mechanism affecting the upward and downward movements of isopycnals is the passage of CTWs. CTWs originating at the equator are well observed by an SLA signal that propagates along the equatorial and coastal waveguides (*18*, *24*). Variations in SLA associated with CTWs are the result of the steric height, which is caused by changes in water-column density. The seasonal maximum and minimum SLA in the tAUS are found at the beginning of the main downwelling and upwelling seasons, respectively (Fig. 1B). However, CTWs are associated with specific spatial (vertical and cross-shelf) structures that define different CTW modes, which propagate with different phase velocities. Such CTW modes can be derived theoretically from the mean stratification and the cross-shelf topography (*17*, *19*, *22*, *23*, *48*). Comparing the observed changes of the cross-shelf density field (Fig. 3C) with the cross-shelf depth structures of density anomaly of the theoretically derived CTW modes (fig. S4) suggests that only high-mode CTWs are capable of explaining the observed seasonal differences. Particularly, CTW modes 4 and 5 agree well with the observed density difference (Fig. 3C) as the depth of the zero crossing (i.e., the depth at which density surfaces do not move) and the depth of maximum density change away from the surface are at comparable depth. This implies that in austral winter the passage of high-mode upwelling CTWs deforms the density field and leads to an upward advection of density surfaces near the shelf break. The nitrate field reflects these vertical motions. Thus, associated with the passage of high-mode upwelling CTWs, we observe enhanced nitrate levels within the euphotic zone and stronger vertical nitrate gradients near the surface.

Analyses of hydrographic, nutrient, and oxygen data suggest that high-mode CTWs play a crucial role in the upward advection of the nitracline. On seasonal timescales, the passage of CTWs is observable in SLA in the tAUS (Fig. 1B) (*9*, *18*). However, the gridded altimetric SLA data mostly capture low-mode CTWs. This is due to the decreasing cross-shelf scales of the SLA structure associated with CTWs for higher CTW modes (fig. S4), suggesting that for a given horizontal resolution of gridded altimetric SLA data [i.e., 100 to 200 km effective spatial resolution (*49*)], low-mode CTWs are predominantly observed. Additionally, the number of zero crossings in the vertical density structure increases for higher CTW modes off the shelf, leading to a cancellation effect when vertically integrating over positive and negative density anomalies to derive the steric height anomaly (fig. S6). Thus, while high-mode CTWs are best represented by density changes in the depth range of the nitracline, low-mode CTWs are depicted in SLA data.

We analyze the relationship between the low-mode CTWs observable in SLA, the displacement of isopycnals observed in hydrographic data, and the peak in NPP (Fig. 4). The depths of the 26 and 27.05 kg m^{-3} isopycnals are highly variable both during individual cruises and between the cruises. Nevertheless, the data show a synchronous heaving of the 26 kg m^{-3} isopycnal and deepening of the 27.05 kg m^{-3} isopycnal after the annual sea level minimum. Note that this movement of the isopycnals is not consistent with the vertical velocity structure of low-mode CTWs, but is consistent with those of higher modes (fig. S5). Furthermore, Fig. 4 shows that these density surfaces reach their seasonal minimum/maximum depth after the minimum in SLA. This suggests that low-mode CTWs observable in SLA are not the primary forcing of the vertical movements of the isopycnals in the upper ocean near the shelf break and ultimately do not control the position of the nitracline. The time delay between the low-mode CTWs observable in SLA and the high-mode CTWs deforming the density field is not clearly determinable from the hydrographic data. The timing of the NPP peak further supports the proposed relationship between low- and high-mode CTWs and their effect on the nitracline, as NPP peaks approximately 40 days after the minimum in SLA.

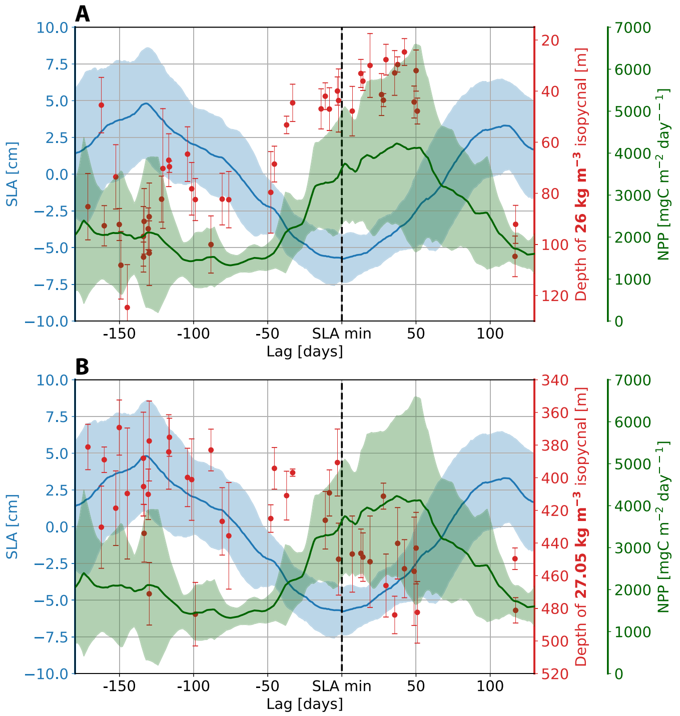

Fig. 4. SLA, NPP, and depth of isopycnals as a function of lag to the time of annual SLA minimum. SLA, NPP, and depth of (**A**) 26 kg m^{-3} and (**B**) 27.05 kg m^{-3} isopycnal as a function of time lag (days) with respect to the time of the annual minimum in SLA occurring during the main upwelling season. Blue lines show the mean SLA for 1995–2022. The timing of the annual SLA minimum is determined using the SLA time series treated with a low-pass filter (cutoff period of 135 days). Green lines show the mean NPP for 2002–2021. Shaded areas show the SDs. Red dots indicate the depth of the respective potential density surface averaged for each cruise considering all CTD profiles taken between 250- and 1000-m water depth. Red bars indicate the SD of the depth of the density surface. Data between 10°S and 12°S are used for all three variables. For both SLA and NPP, data within 1° off the coast are used.

Analysis of velocity data of the upper 500 m observed at a mooring installed at the 1200-m isobath supports the findings from the hydrographic data (fig. S9). Note, however, that the position of the mooring is not ideal for separating different CTW mode contributions, as the velocity variability of the different modes is generally weak at this position. Nevertheless, the observed mean alongshore velocity component as a function of time lag to the annual SLA minimum reveals a signal indicative of a high-mode upwelling CTW arriving about 25 days after the SLA minimum.

The cross-shelf sections of nitrate show that the nitracline not only moves upward between the downwelling and the upwelling seasons but that nitrate-rich water also penetrates far onto the shelf during the upwelling season (Fig. 2). To analyze the onshore transport of nitrate-rich waters, we look at the output of a regional ocean model (fig. S10). In the model, the zonal velocities show onshore currents in the area of the shelf break associated with the passage of CTWs. The onshore flow is strongest at about mid-depth above the upper continental slope and shelf (fig. S10B). Furthermore, onshore velocities peak after the minimum in the SLA.

Overall, the observational data and the model output suggests that CTWs of different vertical structures propagate along the continental shelf in austral winter that are phase-locked to each other. At a given location in the tAUS, the low-mode CTW visible in SLA arrives first. Later (presumably about 25 days), the corresponding high-mode CTW arrives and affects the depth of the nitracline as well as the onshore extent of nitrate-rich waters.

Upward nitrate supply by vertical mixing

Associated with the passage of high-mode CTWs during the upwelling season, nitrate-rich water is advected upward and onto the shelf toward the coast. Previous studies showed that the shelf region of the tAUS is a region of enhanced vertical mixing (*13*, *31*, *32*). Since vertical mixing can influence the nitrate supply to the surface ocean (*50*, *51*), we analyze its effect on the nitrate distribution in the tAUS.

Microstructure profiles collected during six research cruises conducted during different seasons allow us to analyze turbulence at a cross-shelf section at 11°S (*32*). The mean distribution of dissipation rates of TKE reveals a dependence on bathymetry (Fig. 5A) (*32*). Waters shallower than 75 m mark a region of enhanced mixing where dissipation rates above 10^{-6} W kg^{-1} are frequently observed. Since vertical mixing on the shelf of the tAUS is mainly driven by internal tides and the tidal energy available for mixing on the shelf is nearly constant throughout the year (*31*), the mean section of turbulence dissipation rate gives us an estimate of the distribution of mixing on the Angolan shelf at 11°S for the whole year.

To estimate diffusive nitrate fluxes due to vertical mixing in the tAUS, we combine all turbulence dissipation rates and derived eddy diffusivities from the microstructure dataset with the seasonally averaged nitrate gradients (see Materials and Methods). Since the dissipation rates show a dependence on bathymetry, we analyze the turbulent nitrate fluxes as a function of bathymetry by partitioning the data into three depth regions [following the approach of (*32*)]. Vertical diffusive nitrate fluxes are calculated as a function of distance to the mixed layer, since we want to analyze the nitrate flux into the mixed layer from below.

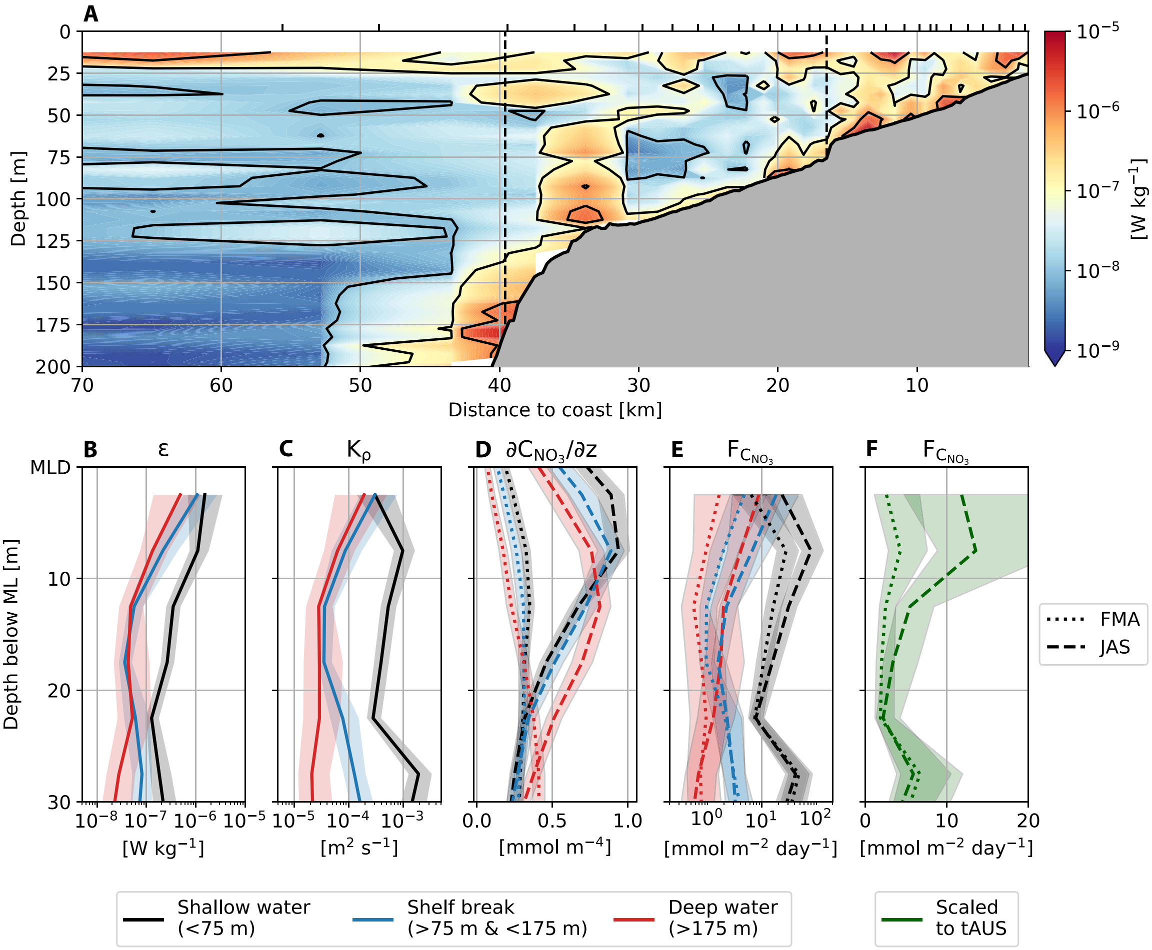

Fig. 5. Vertical mixing and diffusive nitrate fluxes. (**A**) Mean section of dissipation rate of turbulent kinetic energy (TKE) at 11°S as a function of distance to coast from microstructure data. Microstructure data are binned together into groups of 20 profiles, and the spatial extent of the groups is indicated by vertical ticks at the top of the plot. Measurements within the mixed layer and in the upper 10 m were discarded before averaging. Vertical dashed lines separate the three depth regions. (**B** to **E**) Mean profiles taken in shallow water (water depth <75 m, black), in the area of the shelf break (water depth >75 and <175 m, blue), and in deep waters (water depth >175 m, red) as a function of distance to the mixed layer depth. (B) Dissipation rate of TKE (W kg^{-1}). (C) Eddy diffusivity (m^2 s^{-1}). (D) Vertical nitrate gradient (mmol m^{-4}) inferred from oxygen data (see Materials and Methods). (E) Turbulent nitrate flux (mmol m^{-2} day^{-1}). (**F**) Turbulent nitrate flux (mmol m^{-2} day^{-1}) scaled to the whole tAUS. [(D) to (F)] Results for February–April (dotted) and July–September (dashed). Shaded areas indicate 95% confidence intervals. Note the logarithmic scale in (B), (C), and (E).

The vertical nitrate gradient exhibits clear seasonal differences (Fig. 5D). From February to April, the vertical nitrate gradient below the mixed layer is nearly constant, with values between 0.1 and 0.4 mmol m^{-4} within 30-m distance from the mixed layer. In contrast, the vertical nitrate gradient is strongly increased between July and September. There is a clear maximum within 10 m below the mixed layer with values of up to 1 mmol m^{-4}. Furthermore, the vertical nitrate gradient is elevated in shallow waters compared to deeper waters.

The resulting turbulent nitrate fluxes illustrate the temporal and spatial differences (Fig. 5E). The turbulent nitrate flux into the mixed layer can be determined by averaging the profiles between 2 and 15 m below the mixed layer. The highest turbulent nitrate fluxes are estimated during the upwelling season in shallow waters (44.8 [29.5, 75.8] mmol m^{-2} day^{-1}, values in brackets give the 95% confidence interval). The weakest turbulent nitrate fluxes are found during the downwelling season in deep waters (1 [0.5, 2.5] mmol m^{-2} day^{-1}).

These calculations clearly show that turbulent nitrate fluxes are strongly elevated in shallow waters during the upwelling season. However, only a small area within the tAUS has these shallow water depths. To estimate the turbulent nitrate flux over the whole tAUS (8°S to 15°S, 1° distance to the coast), we scale the results found at the 11°S section to the whole tAUS. To do this, we compute a weighted mean based on the area of the tAUS that falls within the respective depth ranges (Fig. 5F). The estimated mean turbulent nitrate flux for February–April is 3.1 [1.9, 5.9] mmol m^{-2} day^{-1} and 10.3 [5.9, 20.8] mmol m^{-2} day^{-1} for July–September. Assuming the validity of the Redfield ratio (C:N ~ 6.6) (*50*) for phytoplankton, this would support a carbon fixation of 307 [188, 578] mgC m^{-2} day^{-1} for February–April and 1007 [574, 1987] mgC m^{-2} day^{-1} for July–September. Thus, the new production due to turbulent nitrate flux supplies about 16% [10%, 30%] during the downwelling phase and about 28% [16%, 55%] during the upwelling phase to the NPP. Note that the NPP is the result of new production due to nutrient input into the euphotic zone and regenerated production due to nutrient recycling in surface waters. The ratio of new and regenerated production is highly variable for each ecosystem (*52*, *53*). Nevertheless, comparisons with potential new production rates in other eastern boundary upwelling regions suggests that turbulent nitrate fluxes play an important role for the NPP signal in the tAUS (*53*).

The turbulent nitrate fluxes calculated here are elevated during the upwelling season compared to the downwelling season. Note that the fluxes presented here are calculated from two datasets that were measured nonsimultaneously and independently of each other, which introduces additional uncertainties. The turbulence dataset was measured during cruises conducted in different seasons. We argue that the dataset can be averaged to provide a good estimation of the distribution of the turbulence dissipation rate at the Angolan shelf that is assumed to be constant throughout the year, as Zeng *et al.* (*31*) showed that tidal energy available for mixing is nearly constant and seasonally independent. Furthermore, the results offer a convincing explanation for the seasonal difference in surface productivity observed in satellite data. The maximum vertical nitrate gradient is stronger during the upwelling season and is located in close proximity to the base of the mixed layer especially in shallow waters. Previous studies of the tAUS have shown that elevated vertical mixing occurs throughout the year and is an important mechanism for cooling the mixed layer near the coast (*31*, *32*). This further suggests that the mixing at the base of the mixed layer acting on different vertical nitrate gradients throughout the year leads to a higher nitrate supply to the surface mixed layer and ultimately to higher NPP in the surface ocean during the austral winter.

Interannual variability of productivity in the tAUS

Satellite data show that the strength of the NPP signal in austral winter is subjected to interannual variability. We now investigate how this variability is related to the amplitude of CTWs arriving from the equatorial region into the tAUS. To estimate the interannual variability of the strength of CTWs and productivity, we rely on satellite data of SLA and NPP, as these datasets provide long time series and are comparable on interannual timescales. For this analysis, we focus on the area from 8°S to 15°S within 1° distance of the coast. We focus on this region to analyze the variability in the tAUS while excluding the direct influence of the Congo River and from the Angola-Benguela frontal zone (Fig. 1B).

SLA data show that the timing of the upwelling CTW varies from year to year. Between 2003 and 2021, the SLA minimum was reached on average on July 21 with an SD of 10 days. To evaluate the strength of the upwelling CTW, we calculate the 3-month mean SLA centered around the annual SLA minimum for each year. We now want to correlate the strength of the SLA signal with the strength of the NPP signal. However, the seasonal cycle of SLA and NPP shows a lag between the two variables (Figs. 4 and 6A). Correlating the 3-month mean SLA with the corresponding 3-month mean NPP at different lags reveals highest correlation with SLA leading NPP by 50 days (fig. S11). The Pearson's correlation coefficient between 3-month mean SLA and 3-month mean NPP lagged by 50 days as shown in Fig. 6B is −0.85, which is significant at the 99% confidence level. During the austral winter, 73% of the variance in the mean NPP signal can be attributed to the variability in the mean amplitude of the SLA. Note that NPP peaks on average on August 27 and thus 37 days after the minimum in SLA. This discrepancy is most likely caused by noise in the NPP data. Note in this context that the NPP data product relies on temporal interpolation to fill gaps due to clouds, which are persistent in austral winter in the tAUS (*54*). Thus, determining the exact lag between the minimum in SLA and the maximum in NPP is ambitious. Nevertheless, the correlation coefficient exceeds −0.8 for SLA leading NPP between 33 and 64 days (fig. S11). This suggests that the strong relationship between mean austral winter SLA and NPP signals presented in Fig. 6 is robust, although the exact lag between the two peaks cannot be determined precisely.

The high correlation between the CTW signal observed in SLA and the corresponding NPP signal emphasizes the crucial role that CTWs play for biological productivity in the tAUS. Generally, years with a strong upwelling CTW signal in SLA in austral winter have higher NPP levels than years with weaker upwelling CTW signals. Between 2003 and 2021, the strongest upwelling CTW signal in SLA is found in 2004 (−6.5 cm), coinciding with the year of the highest NPP peak (4978 mgC m^{-2} day^{-1}). In 2021, the weakest CTW signal (−2.4 cm) is associated with the lowest NPP peak (2337 mgC m^{-2} day^{-1}). Note that the weakest upwelling CTW in 2021 was associated with the 2021 Benguela Niño, an extreme warm event observed by satellite SST in the tAUS (*13*), which peaked anomalously late and significantly reduced the coastal productivity during austral winter (*55*).

The analysis of satellite data reveals a high correlation between the magnitude of the SLA signal of the upwelling CTW in austral winter and the strength of the NPP peak delayed by about 40 days. Thus, years where the SLA signal of the CTW has higher amplitudes tend to have higher NPP. However, analyses of SLA, hydrographic, and mooring data reveal that CTWs visible in SLA are not of the same wave mode as the one displacing the nitracline and thus controlling the productivity. Finally, the high correlation between the amplitude of the low-mode CTWs and the strength of the productivity suggests that the generation mechanism of the high-mode CTWs must be linked to the presence of the low-mode CTWs.

DISCUSSION

The analyses of hydrographic, biogeochemical, ocean turbulence, and satellite data highlight the crucial role of CTWs for the productivity in the tAUS. The main mechanism we propose to explain the seasonal productivity in the tAUS is based on the combined effect of upwelling CTWs and near-coastal mixing, as summarized in the schematic in Fig. 7. In austral winter, different upwelling CTWs are present in the tAUS (Fig. 7A). The arrival of the faster low-mode CTW, which is visible in SLA data, is detected first. With some delay, the slower high-mode CTW, which primarily controls the depth of the nitracline, is observed in the tAUS. This high-mode CTW displaces the nitracline vertically by about 50 m between the main downwelling season and the main upwelling season, thus enhancing nitrate concentration within the euphotic zone. Associated with the passage of CTWs, there is also a horizontal advection of nitrate-rich water toward the coast, ultimately reaching the area of high mixing in shallow waters of the Angolan shelf (Fig. 7B). The presence of nitrate on the shelf, combined with high mixing rates, results in a higher turbulent nitrate flux into the surface mixed layer during the upwelling season compared to the downwelling season when nitrate concentrations on the shelf are low.

Austral winter SLA and NPP correlate on interannual timescales, suggesting a linear relationship between the strength of the upwelling

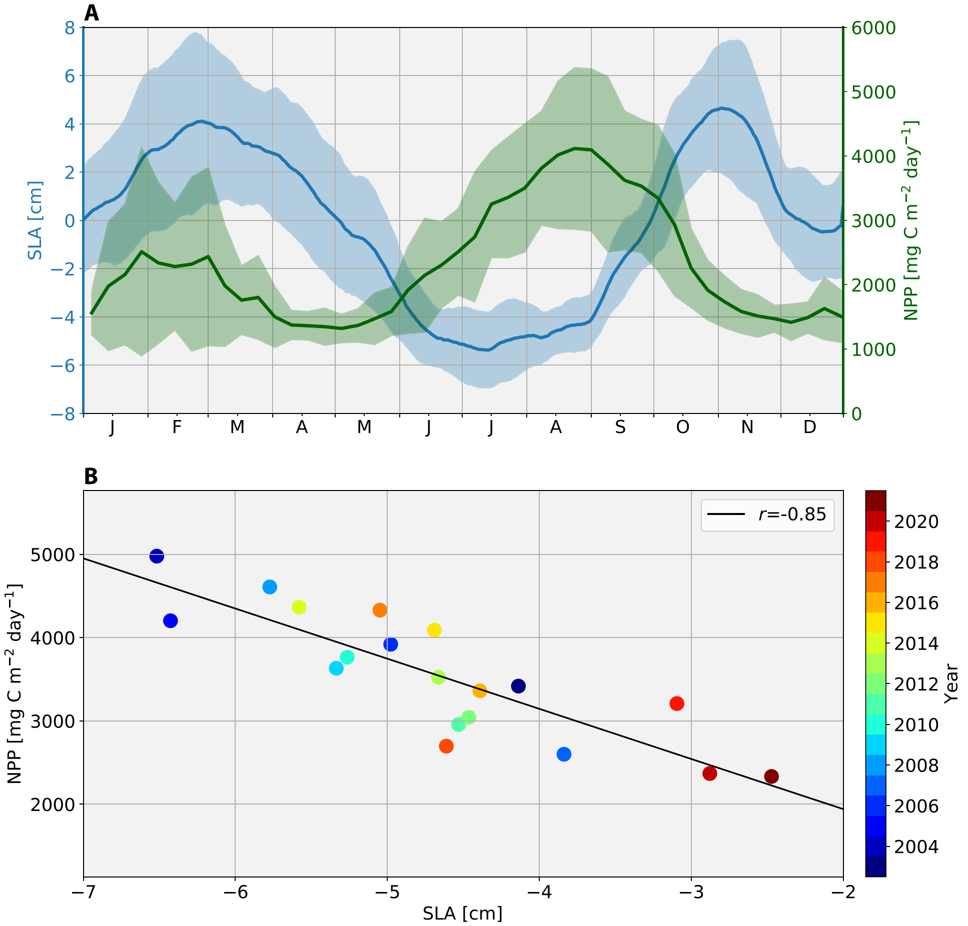

Fig. 6. Seasonal cycle and interannual variability of SLA and NPP. (**A**) Seasonal cycle of SLA (blue) and NPP (green) averaged between 8°S and 15°S within 1° off the coast. Shading indicates the SD. (**B**) Scatterplot of 3-month mean SLA centered around the annual SLA minimum versus 3-month mean NPP lagged by 50 days. The annual minimum of SLA is determined using the SLA time series treated with a low-pass filter (cutoff period is 135 days). Colors indicate the respective year of the data point. Linear regression line and the Pearson's correlation coefficient, *r*, are also given. For both plots, data from 2003–2021 were used.

CTW signal, as observed in SLA and productivity. However, our results also suggest that the low-mode CTWs observed in SLA are not primarily responsible for the uplift of the nitracline. The question naturally arises as to how the low- and high-mode CTWs are related. The strong correlation between the SLA and NPP suggests that the low- and high-mode CTWs are phase-locked.

The velocity and potential density fields of a regional ocean model suggest, similar to the observations, that high-mode CTWs arrive at 11°S after the SLA minimum (Fig. 8B). Isopycnals in the upper ocean reach their seasonal minimum depth after the minimum in SLA. The time lag between the minimum depth of the 26 kg m^{-3} isopycnal and the minimum in SLA is 30 days. Simultaneously, the depth of isopycnals at greater depths increases after the minimum in SLA. The velocity field shows upward propagating wave phases after the arrival of the SLA minimum, indicating downward energy propagation (*56*). We find the signals in the density and velocity field not only at 11°S but also at various latitudes (Fig. 8, A to C). Further south, at 21°S, the signal in the velocity field and the rise of the 26 kg m^{-3} isopycnal is strongly reduced (Fig. 8D). Note that the time lag between low- and high-mode CTW signals is of comparable length between 6°S and 16°S. Ultimately, this suggests that the low- and high-mode CTWs are not waves propagating independently along the African continent as then the lag between the waves would increase southward along the coastal waveguide. Instead, these results suggest that high-mode CTWs are constantly generated with the arrival of low-mode CTWs. This mechanism is also supported by the strong correlation between SLA and NPP, suggesting a strong coupling between low- and high-mode CTWs. The high-mode CTWs can be assumed to not propagate over long distances as they are likely to be highly dissipative (*22*). Open questions remain regarding the origin and energetics of the high-mode CTWs displacing the nitracline and their coupling to the low-mode CTWs. How does energy transfer between low- and high-mode CTWs work? One mechanism that could play a vital role in the forcing of high-mode CTWs is friction. Romea and Allen (*57*) investigated the effect of the bottom Ekman layer on CTWs under different slope conditions. They show that for slopes where the Rossby radius is large compared to the slope width, which is the case in the tAUS, the CTWs are strongly affected by the bottom stress and that the modal structures are altered. They further show that an onshore flow is induced. Thus, this mechanism could potentially explain the forcing of the high-mode CTWs as well as the onshore transport of nitrate-rich waters in the tAUS.

Results of this study show that there is a delay between the minimum in SLA and the rise of the nitracline of the order of ~25 days, and

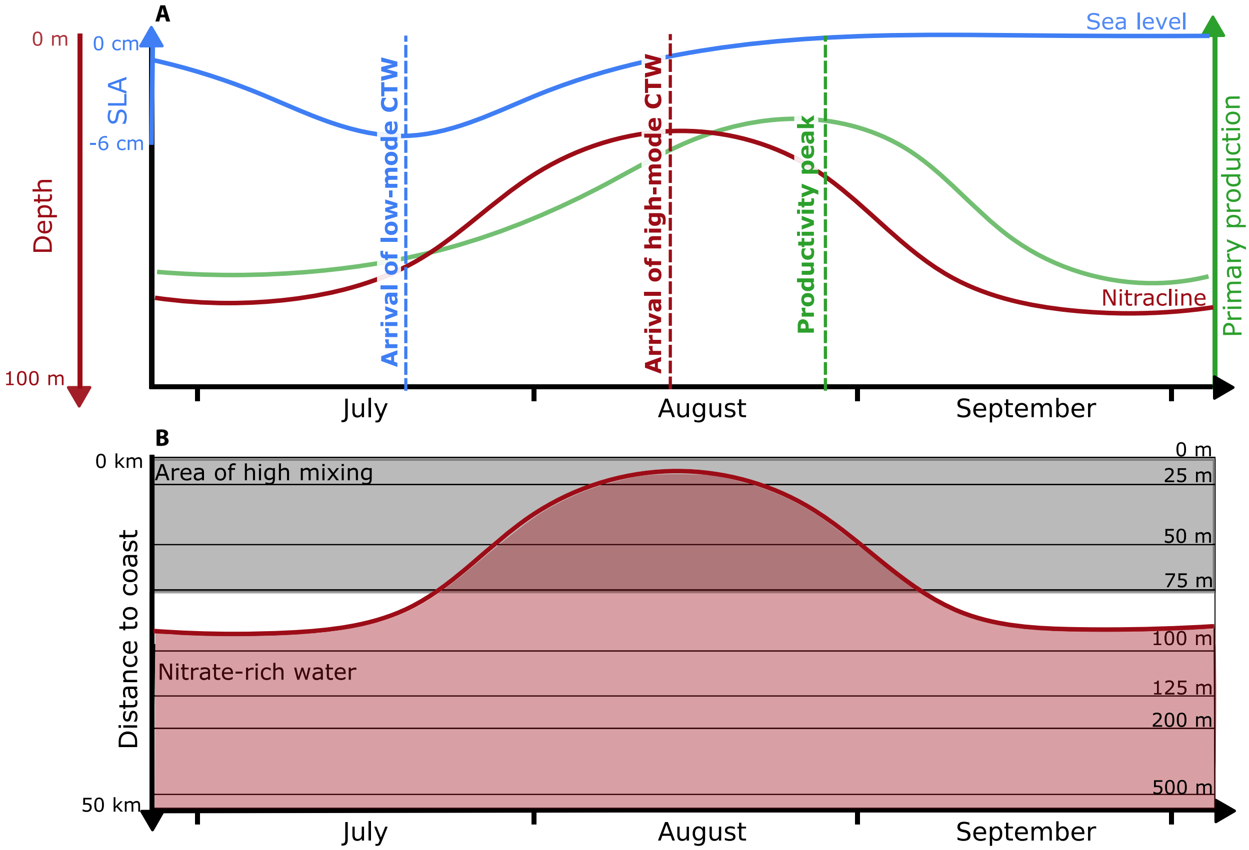

Fig. 7. Schematic view of how CTWs and mixing can explain the high productivity season in the tAUS. (**A**) Time evolution of SLA (blue), nitracline depth (red), and NPP (green) at a location in the tAUS near the shelf break. (**B**) Time evolution of the onshore extent of nitrate-rich water along a cross-shelf section in the tAUS. Gray area marks the area of high mixing. Black lines show the depth contours at 25-m intervals (0 to 125 m) and the 200- and 500-m isobaths. Tick marks on the *x* axes indicate the beginning of the respective month.

that NPP peaks about 40 days after the minimum in SLA. Consequently, this suggests that NPP peaks about 15 days after the nitracline rise. Previous studies showed that the response of biological activity to nutrient supply is faster (*58*, *59*). In the tAUS, the timing between the nitracline uplift and the peak in NPP is likely to be influenced by timescales of vertical mixing and horizontal exchange. The initial upwelling of the nitracline leads to an immediate increase in NPP (Fig. 4). Additionally, we find an enhanced turbulent nitrate flux into the surface ocean in the shallow waters of the tAUS. The nitrate-rich water is likely to be redistributed by small-scale horizontal advection as discussed in (*32*), leading to an increase in NPP further offshore as well. These processes could explain the delay between the uplift of the nitracline and the peak in NPP. However, further work must be done to understand the interplay between these processes. Note that the time lag is of the same order of magnitude as the lag between nitracline upwelling by intraseasonal CTWs and phytoplankton blooms in the Peruvian upwelling system, as found in a modeling study (*42*).

The lag between the SLA signal and the NPP signal, together with the remote equatorial forcing of CTWs, provides a potential for predicting the strength of the austral winter NPP peak. A similar prediction system for SST was suggested for the interannual Benguela Niño and Niña events, which seasonally peak in austral fall (*34*). To exploit the full potential of this mechanism, the cause of the interannual variability of the CTW signal in austral winter needs to be analyzed. Here, both local and remote mechanisms (interannual variability of equatorial winds) need to be considered.

This study focuses on the main productivity season in austral winter. However, a secondary peak in NPP is visible in January to February, which is weaker and restricted to the northern part of the tAUS (Fig. 1B). Interannual variability of this secondary NPP peak is particularly elevated, and the mean value is mostly controlled by strongly enhanced NPP in early 2016 (not shown). Further research has to be conducted to understand the dynamics and variability of the secondary peak of NPP in January to February.

The research presented here suggests that primary production in the tAUS is mainly controlled by CTWs. However, other mechanisms are able to modulate NPP as well. In austral winter, the wind-driven upwelling transport is at its seasonal minimum (Fig. 1C). The relaxation of alongshore winds leads to a reduced offshore Ekman transport. This can prolong the time upwelled nitrate-rich water spends near the surface before being subducted (*60*). This mechanism could further contribute to the enhancement to the nitrate concentration in the nearshore surface ocean. Note again that the mixed layer depth is deepest during the main upwelling season (*32*). Thus, an effect of light limitation on the plankton growth due to changes in mixed layer depth as suggested for the Peruvian upwelling system (*10*) cannot explain the seasonality in NPP in the tAUS.

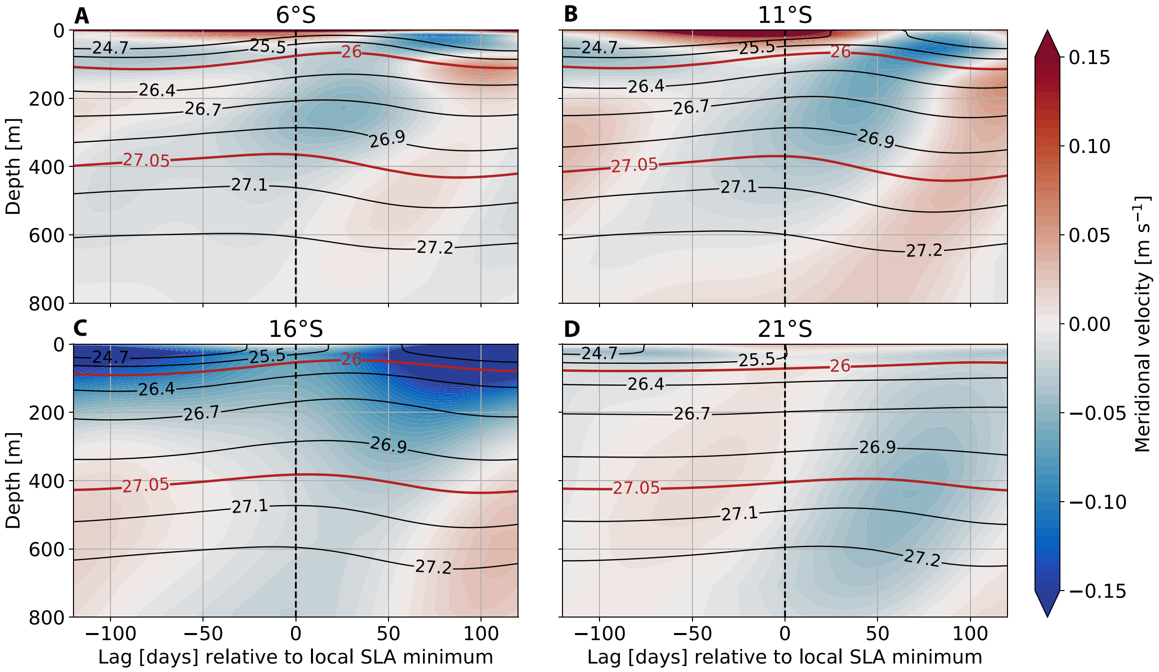

Fig. 8. Meridional velocity and potential density in a regional ocean model. Meridional velocity (colors) and potential density (lines) from the CROCO simulation. Fields are derived at the 800-m isobath for different latitudes as indicated in the titles of (**A** to **D**). The fields are averaged as a function of the lag (days) to the local annual minimum in SLA and are a composite of 58 upwelling seasons. The mean flow is not subtracted; strongest near-surface southward flow is found at 16°S, consistent with the observed latitudinal variation in the strength of the Angola Current (*9*).

This study suggests that CTWs play a crucial role in driving variability in productivity in the tAUS. Understanding how this mechanism behaves under a warming climate is of great socioeconomic importance. Model projections indicate a future weakening of tropical upwelling in the Benguela and Canary upwelling regions, located equatorward of 20°, due to reduced alongshore winds (*5*, *61*). However, as shown here, alongshore winds cannot explain either the seasonal upwelling in the tAUS or its variability. It is therefore necessary to consider other factors in this context. Of particular interest is the possible change in the equatorial trade winds that triggers the remotely forced CTWs.

This study focuses on explaining seasonal productivity in the tAUS. It is of high interest to determine whether similar mechanisms can be observed in other tropical upwelling systems, particularly in the Pacific and the Gulf of Guinea, where semi-annual variability associated with CTWs has been observed (*13*, *62*, *63*). Thus, this work may ignite further research aimed at identifying the role of CTWs and highlighting the importance of CTW modal contributions in other tropical upwelling systems. This, in turn, could ultimately lead to improved seasonal predictions of biological productivity in these highly relevant coastal systems.

MATERIALS AND METHODS

Hydrographic, oxygen, and nitrate data

In this study, we make use of extensive datasets of hydrographic, oxygen, and nitrate data that have been collected in the tAUS (fig. S1 and table S1). Between 1995 and 2015, the EAF Nansen Programme of the Food and Agriculture Organization (FAO) of the United Nations conducted research cruises onboard of the *R/V Dr. Fridtjof Nansen* approximately twice a year (*9*). In most years, the cruises were conducted once during the austral summer (February–April) and once during the austral winter (June–September). During these cruises CTD and oxygen profiles were measured. In total, more than 8000 CTD and oxygen profiles taken in Angolan waters were used. CTD measurements were mostly conducted in shallow waters and near the shelf break. For this study, we use the data collected between 10°S and 11°S (fig. S1).

In addition to the dataset from the Nansen program, we use data from seven research cruises on board of *R/V Meteor* that were conducted in Angolan waters between 2013 and 2022. An overview table of the cruises and the data collected during the cruises used for this study can be found in table S1. During all of these seven cruises, CTD and oxygen profiles were measured. Along with the CTD profiles, discrete water samples were taken for laboratory measurements of nitrate concentration. For the cruises from 2015 onward, continuous nitrate measurements were conducted along with the CTD/oxygen profiles.

Satellite data

Altimetric SLA data are used to analyze the surface signal from CTWs from 1993 to 2021. The SLA data used in this study are from Copernicus DUACS (https://doi.org/10.48670/moi-00148). The daily SLA fields are available with a horizontal resolution of 0.25° × 0.25°. Before conducting the analyses, we removed the mean SLA and detrended the data.

We also use NPP data from Oregon State University to analyze biological activity in the tAUS (http://sites.science.oregonstate.edu/ocean.productivity/index.php). NPP is based on the Eppley vertically generalized production model. It is based on chlorophyll concentration, SST, and photosynthetically available radiation from MODIS. The NPP fields are gap-free and have a horizontal resolution of 1/6°. We use the data between 2002 and 2021.

We calculate the integrated wind-driven upwelling using wind speed data from the cross-calibrated multi-platform (CCMP) product (https://www.remss.com). The six hourly data are available with a horizontal resolution of 0.25° × 0.25° between 1993 and 2019. We subsample the data to daily data before calculating the integrated wind-driven upwelling.

The seasonal cycle of SST shown in Fig. 1 is from the Copernicus OSTIA product (https://doi.org/10.48670/moi-00168) (*64*). The daily temperature fields are available with a horizontal resolution of 0.05° × 0.05°. We use the data from 1993 to 2021.

Mooring data

The CTW signal is analyzed in moored velocity data. The mooring is located at 13°00′E; 10°50′S (77 km offshore) at a water depth of about 1200 m (fig. S1). On the mooring, an upward-looking acoustic Doppler current profiler was installed at 500-m depth to measure the velocity up to 45 m below the sea surface. In this study, we use data collected between July 2013 and April 2022. For more details on the mooring data, see (*30*, *65*).

Calculating nitrate concentration from oxygen data

To understand primary productivity, the distribution of nitrate is of interest. In the tAUS, available nitrate data are restricted to data collected during *R/V Meteor* cruises. In contrast, oxygen data were collected during all CTD stations of *R/V Dr. Fridtjof Nansen* as well. For central water masses, Redfield (*66*) showed that there is a tight relationship between nitrate concentration and oxygen consumption. For the tAUS, we use nitrate data measured from the discrete water samples of CTD profiles and dissolved oxygen concentrations to derive a similar relationship. The apparent oxygen utilization (AOU) is calculated as the difference between the oxygen saturation expected at equilibrium with air for a given temperature and salinity and the measured in situ dissolved oxygen concentration. Oxygen saturation is determined using the Gibbs SeaWater Oceanographic Toolbox (*67*). We use data collected between 8°S and 15°S between 10°E and the African coast in water shallower than 400 m. From these data points, we calculate the relationship using linear regression. The results show the measured data points along with the linear fit, revealing a good correlation between the two variables (fig. S2).

To evaluate the uncertainties of our approach, we compare nitrate concentrations measured by an optical nitrate sensor (SUNA) collected during a subset of the cruises (*R/V Meteor* cruises M131, M148, and M181) to the nitrate values derived from oxygen data. On average, the nitrate concentrations inferred from the oxygen data are 1.8 μmol m^{-3} higher than those measured from the SUNA sensor. The root mean square differences between the two data sets in the upper 400 m after removing the mean bias are 2.4 μmol m^{-3}. Considering the accuracy of the SUNA measurements of about 0.65 μmol m^{-3} (*68*) suggests that nitrate concentrations derived by using AOU here have small uncertainties.

Calculating mean sections from observations

In this study, we use CTD and nitrate profiles inferred from oxygen data to calculate mean cross-shelf sections of nitrate and density with data collected between 10°S and 12°S. The basis for the cross-shelf sections is the mean topography, which we calculate based on the GEBCO topography (http://www.gebco.net). To compute the mean topography, we extract the topography along a line perpendicular to the coast for each latitude grid point of the GEBCO dataset between 10°S and 12°S. The orientation of the coast is calculated by considering the coastline 0.5° around the respective latitude. The topography is then averaged over the latitude. We now divide the mean topography into discrete bins with respect to the water depth and group the observed profiles into these bins. Since there is much more data available on the shelf than further offshore, the bin size increases with distance to the coast. Within 50 km off the coast, the bin size is 5 km, and further offshore, it is 15 km. After averaging the profiles grouped in each bin, we interpolate the data on a regular distance grid and smooth the section by applying a running mean (window size is 7 km).

Turbulent nitrate fluxes

We use ocean turbulence data to estimate turbulent nitrate fluxes in the tAUS (fig. S1). Turbulence was measured using a loosely tethered free-falling microstructure profiler manufactured by Sea&Sun Technology. The profiler was equipped with two to three airfoil shear sensors, an acceleration sensor, tilt sensors, a fast temperature sensor, and standard CTD sensors. We estimate dissipation rates of TKE, ε, from the data from the airfoil shear sensors [for detailed description, see (*32*, *69*)]. For that, we integrate the shear wave number spectrum of overlapping 2-s intervals while assuming isotropy. Loss of shear variance due to the limited resolution in wave number space was accounted for by fitting the spectra to the universal Nasmyth spectrum (*70*) before integration.

To calculate the turbulent nitrate flux into the mixed layer, we map the profiles as a function of depth below the mixed layer. We discard all measurements within the mixed layer and 2 m from the mixed layer as the mixing efficiency is not well defined in low stratified waters (*71*). Additionally, we discarded all measurements in the upper 10 m to exclude ship-induced turbulence. To derive turbulent quantities, we bin the microstructure data in 5-m depth bins with respect to the mixed layer depth. The mixed layer depth is defined as the depth at which the density deviates by 0.125 kg m^{-3} from the surface value. The turbulent eddy diffusivity ($K_\rho = \Gamma\langle\varepsilon\rangle N^{-2}$) is calculated by considering the stratification, defined by the squared Brunt-Väisäla frequency, N^2, within the same depth bins. The mixing efficiency Γ is set to 0.2 (*71*). The vertical nitrate flux is then calculated as $F_{C_{\mathrm{NO_3}}} = K_\rho \frac{\partial C_{\mathrm{NO_3}}}{\partial z}$.

The turbulence data used in this study were collected during six research cruises aboard the *R/V Meteor* (see the Supplementary Materials). These cruises were conducted at different times of the year, not primarily during the main upwelling and downwelling seasons. The primary energy source of vertical mixing in the tAUS is thought to be dissipation of internal tidal energy, where energy available for mixing on the shelf is nearly constant throughout the year (*31*). This is supported by observations, as seasonal differences in the turbulence levels from the available data in the tAUS were not identified (*32*). Therefore, we combine the ocean turbulence data collected during the six cruises on board of *R/V Meteor* with the seasonal gradients of nitrate from all available biogeochemical data. The 701 microstructure profiles provide an estimate of the mean distribution of mixing on the Angolan shelf at 11°S. Since the mean distribution of TKE dissipation rates shows a dependence on bathymetry (Fig. 5) (*32*), we determine mean eddy diffusivities and turbulent nitrate fluxes as a function of bathymetry [following the approach of (*32*)].

To do this, we divide the data into three depth regions: shallow waters (water depths <75 m), the shelf break area (water depths between 75 m and 175 m), and deep waters (water depths >175 m). With mean vertical nitrate gradients calculated for the main downwelling and upwelling seasons, we are able to provide an estimate of the seasonally varying turbulent nitrate flux into the ocean mixed layer.

The uncertainties of the turbulent nitrate fluxes are described in terms of the 95% confidence limits (CL95) [following (*32*, *69*)]. CL95 for the turbulent dissipation rates of TKE are calculated via bootstrapping. CL95 for the Brunt-Väisäla frequency (N^2) and the vertical nitrate gradient $\left(\frac{\partial C_{\mathrm{NO_3}}}{\partial z}\right)$ are calculated by calculating the standard error (SE) and converting the SE to CL95 via $\mathrm{CL95} = \overline{x} \pm 1.96 \cdot \mathrm{SE}$. The uncertainties of the eddy diffusivity (K_ρ) and the turbulent nitrate flux (F_{CNO3}) are given via SE propagation where the uncertainty of the mixing efficiency (Γ) is set to 0.004 [following (*72*)].

Theoretical CTW modes

CTWs are associated with specific spatial structures of the horizontal and vertical velocity components and density fields that can be described as a sum of modes (*17*, *21*). Spatial structures, phase, and group velocities of the respective CTW modes depend on stratification, cross-shore topography, latitude, and mean flow (*17*). Theoretical spatial structures for different CTW modes can be derived by considering a linear, inviscid, hydrostatic, free-surface ocean, for frequencies less than the inertial frequency, horizontally uniform stratification, and an alongshore nonvarying bottom topography (*17*). To derive the CTW modal structures for the tAUS, we use the toolbox developed by Brink and Chapman (*48*), with the mean flow set to zero. We derive the spatial structures and phase speeds of CTW modes at 11°S within a distance of 400 km from the coast using the mean cross shore topography (GEBCO) averaged between 10°S and 12°S. The mean stratification profile is calculated from hydrographic data used in this study (fig. S3).

Regional ocean model configuration

The velocity field and the movement of the potential density surfaces relative to the SLA minimum are analyzed in a regional ocean model. We use the Coastal and Regional Ocean COmmunity (CROCO) model. The model configuration has previously been used to study the dynamics in the eastern-equatorial sector and along the coast of southwest Africa. Comparisons with observations as well as a detailed description of the model setup can be found in (*37*), where the configuration used here is named CROCO$^{\mathrm{LONG}}$. The model spans the tropical Atlantic (30°S to 10°N, 62.25°W to 17.25°E) with a horizontal resolution of 1/12° and 37 terrain-following vertical levels. Model momentum, heat, and freshwater forcings are derived using bulk formulae based on daily surface fields from the DRAKKAR Forcing Set v5.2 (*73*). River runoff is not included in the simulation; instead, the sea surface salinity is restored to CARS2009 climatological sea surface salinity (*74*). After a 5-year spin-up, the model is run for 58 years (1958–2015), during which 3-day averages of the model outputs are stored.

Integrated wind-driven upwelling

To show the influence of the wind-driven upwelling on the tAUS variability, we calculate the seasonal cycle of the integrated wind-driven upwelling following (*75*). It represents the sum of the coastal upwelling due to the coastal divergence of the Ekman transport driven by the meridional (along-shore) wind stress and the wind stress curl–driven upwelling within the coastal box. To do so, we first derive the wind stress from the 10-m wind speed ($\boldsymbol{u}$) using the following bulk formula: $\tau = \rho_a * c_d * |\boldsymbol{u}| * \boldsymbol{u}$, using a reference density $\rho_a = 1.22$ kg m^{-3} and a drag coefficient $c_d = 0.0013$. The integrated wind-driven upwelling is then calculated via $W = -\frac{\tau^y_{x=-L}}{\rho f}$, with $\tau^y_{x=-L}$ being the alongshore wind stress at one degree distance from the coast (extent of the coastal box), $\rho = 1025$ kg m^{-3} a reference density, and f the Coriolis parameter.

Different time periods of observation

In this study, many different observational datasets are used. These datasets cover different time periods, which can introduce uncertainties. For most part of the study, we combine data from the same period to draw the respective conclusions. One exception is the relationship between the low-mode CTWs observable in SLA, the isopycnal displacement calculated from hydrographic data, and NPP (Fig. 4). A sensitivity test revealed that the results are similar even when cutting the data to the same time period (not shown). Note also that we remove the linear trend from all satellite observations before conducting our analyses to remove long-term changes.

Supplementary Materials

This PDF file includes:
Figs. S1 to S11
Table S1
Supplementary text

REFERENCES AND NOTES

1. S. P. Kirkman, L. Blamey, T. Lamont, J. G. Field, G. Bianchi, J. A. Huggett, L. Hutchings, J. Jackson-Veitch, A. Jarre, C. Lett, M. R. Lipiński, S. W. Mafwila, M. C. Pfaff, T. Samaai, L. J. Shannon, Y. J. Shin, C. D. van der Lingen, D. Yemane, Spatial characterisation of the Benguela ecosystem for ecosystem-based management. *African J. Mar. Sci.* **38**, 7–22 (2016).
2. M. Sowman, P. Cardoso, Small-scale fisheries and food security strategies in countries in the benguela current large marine ecosystem (BCLME) region: Angola, Namibia and South Africa. *Mar. Policy* **34**, 1163–1170 (2010).
3. A. Longhurst, Seasonal cooling and blooming in tropical oceans. *Deep. Res. Part I* **40**, 2145–2165 (1993).
4. F. P. Chavez, A. Bertrand, R. Guevara-Carrasco, P. Soler, J. Csirke, The northern Humboldt current system: Brief history, present status and a view towards the future. *Prog. Oceanogr.* **79**, 95–105 (2008).
5. D. Wang, T. C. Gouhier, B. A. Menge, A. R. Ganguly, Intensification and spatial homogenization of coastal upwelling under climate change. *Nature* **518**, 390–394 (2015).
6. A. Bakun, S. J. Weeks, The marine ecosystem off Peru: What are the secrets of its fishery productivity and what might its future hold? *Prog. Oceanogr.* **79**, 290–299 (2008).
7. A. C. Thomas, P. Ted Strub, R. A. Weatherbee, C. James, Satellite views of Pacific chlorophyll variability: Comparisons to physical variability, local versus nonlocal influences and links to climate indices. *Deep. Res. Part II* **77–80**, 99–116 (2012).
8. A. C. Thomas, M. E. Carr, P. T. Strub, Chlorophyll variability in eastern boundary currents. *Geophys. Res. Lett.* **28**, 3421–3424 (2001).
9. P. Tchipalanga, M. Dengler, P. Brandt, R. Kopte, M. Macuéria, P. Coelho, M. Ostrowski, N. S. Keenlyside, Eastern boundary circulation and hydrography off Angola building Angolan oceanographic capacities. *Bull. Am. Meteorol. Soc.* **99**, 1589–1605 (2018).
10. T. Xue, I. Frenger, A. E. F. Prowe, Y. S. José, A. Oschlies, Mixed layer depth dominates over upwelling in regulating the seasonality of ecosystem functioning in the Peruvian upwelling system. *Biogeosciences* **19**, 455–475 (2022).
11. Z. Mao, Z. Mao, C. Jamet, M. Linderman, Y. Wang, X. Chen, Seasonal cycles of phytoplankton expressed by sine equations using the daily climatology from satellite-retrieved chlorophyll-a concentration (1997-2019) over global ocean. *Remote Sens. (Basel)* **12**, 2662 (2020).
12. V. Echevin, O. Aumont, J. Ledesma, G. Flores, The seasonal cycle of surface chlorophyll in the Peruvian upwelling system: A modelling study. *Prog. Oceanogr.* **79**, 167–176 (2008).
13. P. Brandt, G. Alory, F. M. Awo, M. Dengler, S. Djakouré, R. A. Imbol Koungue, J. Jouanno, M. Körner, M. Roch, M. Rouault, Physical processes and biological productivity in the upwelling regions of the tropical Atlantic. *Ocean Sci.* **19**, 581–601 (2023).

14. R. Farneti, A. Stiz, J. B. Ssebandeke, Improvements and persistent biases in the southeast tropical Atlantic in CMIP models. *npj Clim. Atmos. Sci.* **5**, 42 (2022).
15. I. Richter, Climate model biases in the eastern tropical oceans: Causes, impacts and ways forward. *Wiley Interdiscip. Rev. Clim. Chang.* **6**, 345–358 (2015).
16. J. Kurian, P. Li, P. Chang, C. M. Patricola, J. Small, Impact of the Benguela coastal low-level jet on the southeast tropical Atlantic SST bias in a regional ocean model. *Clim. Dyn.* **56**, 2773–2800 (2021).
17. K. H. Brink, A comparison of long coastal trapped wave theory with observation off Peru. *J. Phys. Oceanogr.* **12**, 987–913 (1982).
18. I. Polo, A. Lazar, B. Rodriguez-Fonseca, S. Arnault, Oceanic Kelvin waves and tropical Atlantic intraseasonal variability: 1. Kelvin wave characterization. *J. Geophys. Res. Ocean.* **113**, 1–18 (2008).
19. K. H. Brink, Energy conservation in coastal-trapped wave calculations. *J. Phys. Oceanogr.* **19**, 1011–1016 (1989).
20. A. J. Clarke, K. H. Brink, The response of stratified, frictional flow of shelf and slope waters to fluctuating large-scale, low-frequency wind forcing. *J. Phys. Oceanogr.* **15**, 439–453 (1985).
21. A. J. Clarke, Observational and numerical evidence for wind-forced coastal trapped long waves. *J. Phys. Oceanogr.* **7**, 231–247 (1977).
22. S. Illig, E. Cadier, M.-L. Bachèlery, M. Kersalé, Subseasonal coastal-trapped wave propagations in the Southeastern Pacific and Atlantic Oceans: 1. A new approach to estimate wave amplitude. *J. Geophys. Res. Ocean.* **123**, 3915–3941 (2018).
23. S. Illig, M.-L. Bachèlery, E. Cadier, Subseasonal coastal-trapped wave propagations in the Southeastern Pacific and Atlantic Oceans: 2. Wave characteristics and connection with the equatorial variability. *J. Geophys. Res. Ocean.* **123**, 3942–3961 (2018).
24. M. Rouault, Bi-annual intrusion of tropical water in the northern Benguela upwelling. *Geophys. Res. Lett.* **39**, 2–7 (2012).
25. R. Kopte, P. Brandt, M. Claus, R. J. Greatbatch, M. Dengler, Role of equatorial basin-mode resonance for the seasonal variability of the Angola current at 11°S. *J. Phys. Oceanogr.* **48**, 261–281 (2018).
26. P. Brandt, M. Claus, R. J. Greatbatch, R. Kopte, J. M. Toole, W. E. Johns, C. W. Böning, Annual and Semiannual cycle of equatorial atlantic circulation associated with Basin-mode resonance. *J. Phys. Oceanogr.* **46**, 3011–3029 (2016).
27. S. G. H. Philander, R. C. Pacanowski, Response of equatorial oceans to periodic forcing. *J. Geophys. Res. Ocean.* **86**, 1903–1916 (1981).
28. V. Thierry, A. M. Treguier, H. Mercier, Numerical study of the annual and semi-annual fluctuations in the deep equatorial Atlantic Ocean. *Ocean Model.* **6**, 1–30 (2004).
29. M. Ostrowski, J. C. B. Da Silva, B. Bazik-Sangolay, The response of sound scatterers to El Niño- and La Niña-like oceanographic regimes in the southeastern Atlantic. *ICES J. Mar. Sci.* **66**, 1063–1072 (2009).
30. R. Kopte, P. Brandt, P. C. M. Tchipalanga, M. Macueria, M. Ostrowski, The Angola current: Flow and hydrographic characteristics as observed at 11°S. *J. Geophys. Res. Ocean.* **122**, 1177–1189 (2017).
31. Z. Zeng, P. Brandt, K. G. Lamb, R. J. Greatbatch, M. Dengler, M. Claus, X. Chen, Three-dimensional numerical simulations of internal tides in the angolan upwelling region. *J. Geophys. Res. Ocean.* **126**, e2020JC016460 (2021).
32. M. Körner, P. Brandt, M. Dengler, Seasonal cycle of sea surface temperature in the tropical Angolan upwelling system. *Ocean Sci.* **19**, 121–139 (2023).
33. L. V. Shannon, A. J. Boyd, G. B. Brundrit, J. Taunton-Clark, on the Existence of an El Niño-type Phenomenon in the Benguela System. *J. Mar. Res.* **44**, 495–520 (1986).
34. R. A. Imbol Koungue, S. Illig, M. Rouault, Role of interannual Kelvin wave propagations in the equatorial Atlantic on the Angola Benguela Current system. *J. Geophys. Res. Ocean.* **122**, 4685–4703 (2017).
35. R. A. Imbol Koungue, M. Rouault, S. Illig, P. Brandt, J. Jouanno, Benguela Niños and Benguela Niñas in forced ocean simulation from 1958 to 2015. *J. Geophys. Res. Ocean.* **124**, 5923–5951 (2019).
36. J. F. Lübbecke, C. W. Böning, N. S. Keenlyside, S. P. Xie, On the connection between Benguela and equatorial Atlantic Niños and the role of the South Atlantic Anticyclone. *J. Geophys. Res. Ocean.* **115**, 1–16 (2010).
37. S. Illig, M.-L. Bachèlery, J. F. Lübbecke, Why do Benguela Niños lead Atlantic Niños? *J. Geophys. Res. Ocean.* **125**, E2019jC016003 (2020).
38. M.-L. Bachèlery, S. Illig, M. Rouault, Interannual coastal trapped waves in the Angola-Benguela upwelling system and Benguela Niño and Niña events. *J. Mar. Syst.* **203**, 103262 (2020).
39. M.-L. Bachèlery, S. Illig, I. Dadou, Interannual variability in the South-East Atlantic Ocean, focusing on the Benguela upwelling system: Remote versus local forcing. *J. Geophys. Res. Ocean.* **121**, 284–310 (2016).
40. J. F. Lübbecke, P. Brandt, M. Dengler, R. Kopte, J. Lüdke, I. Richter, M. Sena Martins, P. C. M. Tchipalanga, Causes and evolution of the southeastern tropical Atlantic warm event in early 2016. *Clim. Dyn.* **53**, 261–274 (2019).
41. I. Richter, S. K. Behera, Y. Masumoto, B. Taguchi, N. Komori, T. Yamagata, On the triggering of Benguela Niños: Remote equatorial versus local influences. *Geophys. Res. Lett.* **37**, 1–6 (2010).
42. V. Echevin, A. Albert, M. Lévy, M. Graco, O. Aumont, A. Piétri, G. Garric, Intraseasonal variability of nearshore productivity in the Northern Humboldt Current System: The role of coastal trapped waves. *Cont. Shelf Res.* **73**, 14–30 (2014).
43. J. Lüdke, M. Dengler, S. Sommer, D. Clemens, S. Thomsen, G. Krahmann, A. W. Dale, E. P. Achterberg, M. Visbeck, Influence of intraseasonal eastern boundary circulation variability on hydrography and biogeochemistry off Peru. *Ocean Sci.* **16**, 1347–1366 (2020).
44. M. Ostrowski, B. Bazika-Sangolay, On physical mechanisms controlling inshore aggregations of small pelagic fish in a tropical upwelling system, in *2015 IEEE/OES Acoustics in Underwater Geosciences Symposium (RIO Acoustics)* (IEEE, 2015), pp. 1–7.
45. J. K. Moore, S. C. Doney, K. Lindsay, Upper ocean ecosystem dynamics and iron cycling in a global three-dimensional model. *Global Biogeochem. Cycles* **18**, 1–21 (2004).
46. T. J. Browning, E. P. Achterberg, I. Rapp, A. Engel, E. M. Bertrand, A. Tagliabue, C. M. Moore, Nutrient co-limitation at the boundary of an oceanic gyre. *Nature* **551**, 242–246 (2017).
47. F. M. Awo, M. Rouault, M. Ostrowski, F. S. Tomety, C. Y. Da-Allada, J. Jouanno, J., Seasonal cycle of sea surface salinity in the Angola upwelling system. *J. Geophys. Res. Ocean* **127**, e2022JC018518 (2022).
48. K. H. Brink, D. C. Chapman, *Programs for Computing Properties of Coastal-Trapped Waves and Wind-Driven Motions over the Continental Shelf and Slope* (Woods Hole Oceanographic Institution, 1987).
49. M. Ballarotta, C. Ubelmann, M.-I. Pujol, G. Taburet, F. Fournier, J.-F. Legeais, Y. Faugère, A. Delepoulle, D. Chelton, G. Dibarboure, N. Picot, On the resolutions of ocean altimetry maps. *Ocean Sci.* **15**, 1091–1109 (2019).
50. J. Schafstall, M. Dengler, P. Brandt, H. Bange, Tidal-induced mixing and diapycnal nutrient fluxes in the Mauritanian upwelling region. *J. Geophys. Res. Ocean.* **115**, 1–19 (2010).
51. F. Cyr, D. Bourgault, P. S. Galbraith, M. Gosselin, Turbulent nitrate fluxes in the Lower St. Lawrence Estuary, Canada. *J. Geophys. Res. C Ocean* **120**, 2308–2330 (2015).
52. R. W. Eppley, B. J. Peterson, Particulate organic matter flux and planktonic new production in the deep ocean. *Nature* **282**, 677–680 (1979).
53. M. Messié, F. P. Chavez, Seasonal regulation of primary production in eastern boundary upwelling systems. *Prog. Oceanogr.* **134**, 1–18 (2015).
54. A. Modi, M. K. Roxy, S. Ghosh, Gap-filling of ocean color over the tropical Indian Ocean using Monte-Carlo method. *Sci. Rep.* **12**, 1–11 (2022).
55. S. Illig, M.-L. Bachèlery, The 2021 Atlantic Niño and Benguela Niño Events: External forcings and air–sea interactions. *Clim. Dyn.* **61**, (2023).
56. A. E. Gill, *Atmosphere-Ocean Dynamics* (Academic Press, 1982), vol. 30.
57. R. D. Romea, J. S. Allen, The effect of friction and topography on coastal internal Kelvin waves at low latitudes. *Tellus A Dyn. Meteorol. Oceanogr.* **36**, 384–400 (2022).
58. A. Ferreira, C. Sá, N. Silva, C. Beltrán, A. M. Dias, A. C. Brito, Phytoplankton response to nutrient pulses in an upwelling system assessed through a microcosm experiment (Algarrobo Bay, Chile). *Ocean Coast. Manag.* **190**, 105167 (2020).
59. Y. Collos, Time-lag algal growth dynamics: Biological constraints on primary production in aquatic environments. *Mar. Ecol. Prog. Ser.* **33**, 193–206 (1986).
60. S. Thomsen, X. Capet, V. Echevin, Competition between Baroclinic instability and Ekman Transport under Varying Buoyancy forcings in Upwelling systems: An idealized analog to the Southern Ocean. *J. Phys. Oceanogr.* **51**, 3347–3364 (2021).
61. A. Sylla, J. Mignot, X. Capet, A. T. Gaye, Weakening of the Senegalo–Mauritanian upwelling system under climate change. *Clim. Dyn.* **53**, 4447–4473 (2019).
62. O. Pizarro, G. Shaffer, B. Dewitte, M. Ramos, Dynamics of seasonal and interannual variability of the Peru-Chile undercurrent. *Geophys. Res. Lett.* **29**, 22–24 (2002).
63. F. Gómez-Valdivia, A. Parés-Sierra, A. Laura Flores-Morales, Semiannual variability of the California undercurrent along the Southern California Current System: A tropical generated phenomenon. *J. Geophys. Res. Ocean.* **122**, 1574–1589 (2017).
64. S. Good, E. Fiedler, C. Mao, M. J. Martin, A. Maycock, R. Reid, J. Roberts-Jones, T. Searle, J. Waters, J. While, M. Worsfold, The current configuration of the OSTIA system for operational production of foundation sea surface temperature and ice concentration analyses. *Remote Sens. (Basel)* **12**, 4 (2020).
65. R. A. Imbol Koungue, P. Brandt, Impact of intraseasonal waves on Angolan warm and cold events. *J. Geophys. Res. Ocean.* **126**, e2020JC017088 (2021).
66. A. C. Redfield, *On the Proportions of Organic Derivatives in Sea Water and Their Relation to the Composition of Plankton* (University Press of Liverpool, 1934).
67. T. J. McDougall, P. M. Barker, Getting started with TEOS-10 and the Gibbs Seawater (GSW) oceanographic toolbox. *Scor/Iapso WG* **127**, 1–28 (2011).
68. C. M. Sakamoto, K. S. Johnson, L. J. Coletti, Improved algorithm for the computation of nitrate concentrations in seawater using an in situ ultraviolet spectrophotometer. *Limnol. Oceanogr. Methods* **7**, 132–143 (2009).
69. R. Hummels, M. Dengler, P. Brandt, M. Schlundt, Diapycnal heat flux and mixed layer heat budget within the Atlantic Cold Tongue. *Clim. Dyn.* **43**, 3179–3199 (2014).
70. F. Wolk, H. Yamazaki, L. Seuront, R. G. Lueck, A new free-fall profiler for measuring biophysical microstructure. *J. Atmos. Ocean. Technol.* **19**, 780–793 (2002).
71. M. C. Gregg, E. A. D'Asaro, J. J. Riley, E. Kunze, Mixing efficiency in the ocean. *Ann. Rev. Mar. Sci.* **10**, 443–473 (2018).

72. L. S. T. Laurent, R. W. Schmitt, The contribution of salt fingers to vertical mixing in the North Atlantic tracer release experiment. *J. Phys. Oceanogr.* **29**, 1404–1424 (1999).
73. R. Dussin, B. Barnier, L. Brodeau, J. M. Molines, The making of Drakkar forcing set DFS5. *DRAKKAR/MyOcean Rep. 01-04-16, LGGE, Grenoble, Fr.* (2016).
74. J. Dunn, *CARS 2009: CSIRO Atlas of Regional Seas* (CSIRO, 2009).
75. M. H. Bordbar, V. Mohrholz, M. Schmidt, The relation of wind-driven coastal and offshore upwelling in the Benguela upwelling system. *J. Phys. Oceanogr.* **51**, 3117–3133 (2021).

Acknowledgments: We thank the captains, crews, scientists, and technicians involved in several research cruises in the tropical Atlantic who contributed to collecting data used in this study. **Funding:** The study was funded by EU H2020 under grant agreement 817578 (TRIATLAS project). It was further supported by the German Federal Ministry of Education and Research as part of the SACUS (03G0837A), SACUS II (03F0751A), and BANINO (03F0795A) projects and by the German Science Foundation through several research cruises with *R/V Meteor*. M.-L.B. has received funding from the European Union's Horizon 2020 Research and Innovation Program for the project BENGUP under the Marie Skłodowska-Curie grant agreement ID 101025655. A.S. was supported by NASA grant 80NSSC21K0439, funding from the G. Unger Vetlesen Foundation, and a fellowship from Columbia University's Center for Climate and Life. Model computations were performed on CALMIP computer at University Paul Sabatier (Toulouse, France, CALMIP, project 19002). **Author contributions:** Conceptualization: M.K., P.B., and M.D. Data curation: M.K., M.D., G.K., and S.I. Formal analysis: M.K. Methodology: M.K., P.B., S.I., and M.D. Visualization: M.K. Supervision: P.B. and M.D. Writing—original draft: M.K. Writing—review and editing: M.K., P.B., S.I., M.D., A.S., M.-L.B., and G.K. **Competing interests:** The authors declare that they have no competing interests. **Data and materials availability:** The sea level anomaly data used in this study can be accessed via the Copernicus Server (https://doi.org/10.48670/moi-00148). The net primary production dataset is available online at http://orca.science.oregonstate.edu/1080.by.2160.8day.hdf.eppley.m.chl.m.sst.php. CCMP Version-3.0 vector wind analyses are produced by Remote Sensing Systems. Data are available at www.remss.com. The OSTIA sea surface temperature dataset can be accessed via the Copernicus Server (https://doi.org/10.48670/moi-00168). The hydrographic and biogeochemical data collected on board of *R/V Dr. Fridtjof Nansen* used in this study are available at https://doi.org/10.1594/PANGAEA.886492. The hydrographic, oxygen, and nitrate data collected on board of *R/V Meteor* used in this study are available at https://doi.org/10.5281/zenodo.10062790. The microstructure data are available at https://doi.pangaea.de/10.1594/PANGAEA.953869. The mooring data are available at https://doi.org/10.5281/zenodo.10062790. The model output is available at https://doi.org/10.5281/zenodo.10062790. All necessary code for the data analysis and the preparation of the figures are available at https://doi.org/10.5281/zenodo.10062790.

Submitted 12 July 2023
Accepted 27 December 2023
Published 26 January 2024
10.1126/sciadv.adj6686